Nuclear Science and Techniques (2026) 37:21
https://doi.org/10.1007/s41365-025-01842-w

Numerical study on pebble-bed powder migration and clogging mechanism with purge gas

Xue-Tao Cui[1] · Qi-Gang Wu[1,2] · Jian Wang[2] · Ming-Zhun Lei[2] · Yun-Tao Song[2]

Received: 10 June 2024 / Revised: 2 September 2024 / Accepted: 9 September 2024 / Published online: 2 January 2026

Abstract

As the primary functional component of a fusion reactor, the fusion blanket pebble bed, composed of numerous particles, is crucial for tritium breeding, neutron multiplication, and radiation shielding. Particles within tritium-breeding pebble beds are subjected to prolonged neutron irradiation, high thermal loads, and strong magnetic fields in fusion environments. Such conditions render them susceptible to pulverization and fragmentation. The resulting fragments and powders migrate and are deposited into the gas channel, driven by the purge gas. The reduction in the effective flow area of the gas increases the flow resistance, resulting in tritium retention, degraded heat transfer, and other adverse effects. These conditions impair the thermodynamic properties of the pebble beds and hinder the self-maintenance of tritium. Limited information exists on powder migration and clogging mechanisms in fusion blanket pebble beds, particularly under diverse physical conditions. The aim of this study was to use a computational fluid dynamics model coupled with the discrete element method (CFD-DEM) to numerically explore powder migration and clogging in pebble beds. The model considers factors such as breeder orientation, purge velocity, powder size distribution, and friction coefficient. We propose two migration and clogging mechanisms. One involves powder with a large particle size, and the other does not. The results indicate that the powder migration velocity progresses through three stages: rapid decay, linear decay, and stability. Pebble-bed clogging manifests in two forms: extensive superficial clogging and uniform internal clogging. Two fitted curves were used to depict the migration and clogging tendencies. The powder size distribution significantly influenced the powder migration. The breeder orientation, powder size, and friction coefficient affected the distribution of the clogging powders. However, the impact of the purge velocity on powder migration and clogging in pebble beds was limited, and this effect varied significantly with different particle size ratios. Based on the analysis, a formula is proposed to characterize the behavior of the powder in the pebble beds. The results of this study can aid in analyzing and predicting powder dynamics in pebble beds.

Keywords Coupled CFD-DEM · Pebble beds · Purge gas · Powder flow · Migration and clogging mechanism

1 Introduction

As the primary functional part of a fusion reactor, the fusion blanket is responsible for radiation shielding and tritium self-sufficiency [1–3]. Based on the morphology of the tritium breeder, fusion blankets can be classified into solid- or liquid-breeder blankets. A solid breeder blanket is viewed as a leading candidate for fusion blanket design [4, 5]. Both water-cooled ceramic breeding (WCCB) and helium-cooled ceramic breeding (HCCB) blanket designs utilize solid ceramic pebble beds with numerous particles. For the WCCB blanket, Li_2TiO_3 and $Be_{12}Ti$ act as the breeder and multiplier, respectively, whereas the HCCB blanket employs Li_4SiO_4 and Be. Numerous experimental [6–8] and numerical [9–12] studies have explored the thermohydraulic behavior of pebble beds. However, much of the research on fusion blanket pebble beds has focused on quasi-static conditions. The effects of neutron irradiation, high thermal loads, and strong magnetic fields [13] on pebble beds, which lead to pulverization and fragmentation, are only partially understood. Breeder particle fragments and powders migrate to,

✉ Ming-Zhun Lei
leimz@ipp.ac.cn

[1] School of Nuclear Science and Technology, University of Science and Technology of China, Hefei 230036, China

[2] Institute of Plasma Physics, Chinese Academy of Sciences, Hefei 230031, China

deposit in, and accumulate within gas channels, driven by the purging action. This accumulation diminishes the effective flow area of the purge gas, leading to increased flow resistance and deteriorated gas flow distribution. These issues, including tritium retention and heat transfer degradation, seriously impair the thermodynamic properties of the pebble beds and obstruct tritium self-sustainability [14, 15]. Therefore, predicting and controlling particle powder migration and clogging are essential for reliable tritium extraction and energy conversion efficiency in fusion reactor ceramic pebble beds.

Some studies have focused on particle clogging in porous media. Liu et al. [16] investigated the particle clogging mechanisms through microfluidic chip tests. They classified the clogging mechanisms as dependent (involving one or more adjacent pores) or independent (without adjacent channel involvement). During seepage tests with river sand-filled columns, Ye et al. [17] identified three types of particle clogging: surface interception, internal clogging, and adhesion. Research has often focused on the median particle size ratio of fillers to fine particles as a key clogging factor [18–20]. Tan et al. [21] developed an empirical formula based on the Kozeny–Carmen equation to theoretically predict permeability reduction in permeable bases. Sun et al. [22] reviewed the research on the generation, distribution, radioactivity, deposition, resuspension, and coagulation of graphite dust in a pebble-bed high-temperature reactor. Numerical simulation methods have been utilized to explore the hydraulic behavior and water quality performance of pervious pavements. An advanced computational fluid dynamics model coupled with the discrete element method (CFD-DEM) was developed and validated to assess the permeability of pervious concrete [23–26]. The CFD-DEM coupled method was first proposed by Tsuji et al. [27] and has since been adopted in many investigations in packed beds [28–33]. These research results proved that CFD-DEM is a valid method for simulating and observing two-phase packed-bed systems.

However, few studies have addressed powder flow under a purge gas in the pebble bed of a fusion blanket. Numerous factors can affect the flow characteristics of the powders, and more parameters should be studied to obtain a thorough understanding. The existing models fall short and offer limited predictive insights into powder transport, clogging, and interstitial purge gas dynamics. As a result, the influence of purge gas on particle migration and clogging within pebble beds remains poorly understood. Furthermore, a theoretical basis for understanding the transition from particle migration to clogging in porous media is lacking. Therefore, in this study, coupled CFD-DEM was employed for a numerical investigation of powder migration and clogging, considering factors such as breeder orientation, purge velocity, powder size distribution, and friction coefficient. The primary aim was to elucidate the mechanism of powder migration and clogging within fusion blanket pebble beds. From these numerical findings, a preliminary model for migration and clogging was formulated. The results of this study can aid in analyzing and predicting powder dynamics, as well as analyzing pebble-bed reactors.

The remainder of this paper is organized as follows: Section 2 outlines the numerical methodologies, covering the governing equations, coupling procedures, validation, construction of the pebble-bed models in DEM, and reconstruction using CFD. Section 3 presents and discusses the simulation results, including the effects of breeder orientation, purge velocity, powder size distribution, and friction coefficient on migration and clogging, as well as the mechanism, characterization, and numerical modeling of these processes.

2 Numerical model and validation

2.1 Numerical methodology in the CFD-DEM model

In the CFD-DEM model, the flow in the entire flow region is calculated from the continuity and Navier–Stokes equations, with a porosity term and an additional body-force term used to account for the presence of particles in the fluid. These are given by [34, 35]

$$\frac{\partial(\varepsilon\rho)}{\partial t} + \nabla\cdot(\varepsilon\rho U^{\mathrm{f}}) = 0, \tag{1}$$

$$\frac{\partial(\varepsilon\rho U^{\mathrm{f}})}{\partial t} + \nabla\cdot(\varepsilon\rho\, U^{\mathrm{f}}U^{\mathrm{f}}) = -\varepsilon\nabla p + \varepsilon\nabla\cdot(\mu\nabla U^{\mathrm{f}}) + \varepsilon\rho g - F_{\mathrm{p}\to\mathrm{f}}, \tag{2}$$

$$\varepsilon = \frac{V_0 - V_{\mathrm{p}}}{V_0}, \tag{3}$$

where ε, ρ, U^{f}, p are the volume factor of the gas phase (porosity), density, velocity, and pressure, respectively; V_0 and V_{f} are apparent volume and total particle volume. μ is the viscosity. $F_{\mathrm{p}\to\mathrm{f}}$ is the interphase force exerted by the pebble bed in the lattice on the helium; the main consideration here is the drag force. For gas–particle interactions, the ratio of buoyancy to gravity is on the order of 10^{-3}; therefore, buoyancy can usually be ignored.

The porosity and body force of the fluid mesh elements are determined using the DEM. The equations of motion for the particles include an additional force term that considers their interaction with the fluid. The equations [36, 37] are

$$m_i\frac{\mathrm{d}U_i^{\mathrm{p}}}{\mathrm{d}t} = \sum_{j=1}^{n_i^{\mathrm{c}}} F_{ij}^{\mathrm{c}} + F_i^{\mathrm{g}} + F_i^{\mathrm{f}}, \tag{4}$$

$$I_i \frac{\mathrm{d}\omega_i^{\mathrm{p}}}{\mathrm{d}t} = \sum_{j=1}^{n_i^{\mathrm{c}}} M_{ij}^{\mathrm{c}}, \tag{5}$$

where m_i, U_i^{p}, ω_i^{p} are the particle mass, velocity, and angular velocity, respectively; F_i^{f} is the fluid–particle interaction force; F_{ij}^{c} and M_{ij}^{c} are the contact force and moment between particle i and j, respectively; F_i^{g} is the body force, including gravity and drag force; and I_i is the particle moment inertia.

The force that occurs during the interaction between a particle and a fluid can be characterized by a combination of drag, pressure gradient, viscous tensor gradient, and various other forces. When considering a system comprising gas and particles, the predominant factor influencing the interaction between the fluid and pebble bed is the drag force, which has a significant impact on the precision of the coupled CFD-DEM model. Consequently, achieving an accurate representation of the interphase forces experienced by particles and fluid is essential for CFD-DEM simulations. The interphase force, denoted by $\mathbf{F}_{\mathrm{p}\to\mathrm{f}}$, can be mathematically described as [38]:

$$\mathbf{F}_{\mathrm{p}\to\mathrm{f}} = -\frac{1}{V_{\mathrm{cell}}} \sum_{i=1}^{n_{\mathrm{p}}} F_i^{\mathrm{f}\to\mathrm{p}}, \tag{6}$$

$$F_i^{\mathrm{f}\to\mathrm{p}} = \frac{1}{2} C_{\mathrm{d}} \rho A_i |U_{\mathrm{f}} - U_{\mathrm{p}}| (U_{\mathrm{f}} - U_{\mathrm{p}}), \tag{7}$$

where V_{cell} is the volume of the grid, n_{p} represents the number of particles in the pebble beds, $F_i^{\mathrm{f}\to\mathrm{p}}$ denotes the drag force of helium on each particle, A_i is the projected area of the particle along the direction of helium flow, and C_{d} is the coefficient of drag force. In this study, the Gidaspow model [39] was used to describe the drag coefficient, which can be regarded as a combination of the Wen-Yu model [40] and the Ergun equation [41]. The Gidaspow drag model has a wide range of applications and high calculation accuracy, especially for a dense phase gas–solid pebble bed. C_{d} takes the following form:

$$C_{\mathrm{d}} = \begin{cases} \frac{24}{\varepsilon Re_{\mathrm{s}}}[1 + 0.15(\varepsilon Re_{\mathrm{s}})^{0.687}], & \varepsilon > 0.8 \\ \frac{200(1-\varepsilon)}{\varepsilon Re_{\mathrm{s}}} + \frac{7}{3}, & \varepsilon \le 0.8 \end{cases} \tag{8}$$

$$Re_{\mathrm{s}} = \frac{\rho d_{\mathrm{p}} |U_{\mathrm{f}} - U_{\mathrm{p}}|}{\mu_{\mathrm{f}}} \tag{9}$$

Two-way coupling between the DEM and CFD is numerically achieved by solving Eqs. (1)–(3) using the CFD code and Eqs. (4)–(9) using the DEM code. The DEM determines the porosity and interaction force, which are then normalized by the volume obtained from CFD. CFD calculates the fluid velocity and pressure for each element and subsequently shares these data with the DEM during each exchange. The computational time steps used for the fluid and powders are 6.0×10^{-6} s and 6.0×10^{-8} s, respectively.

For the particle phase, Li et al. [42] suggested a critical time step based on the time required for a Rayleigh wave to propagate along the smallest particle:

$$\Delta t_{\mathrm{DEM}} < \frac{\pi R_{\mathrm{min}}}{0.1631\nu + 0.8766} \sqrt{\frac{2\rho_{\mathrm{s}}(1+\nu)}{\mathrm{E}}}, \tag{10}$$

where Δt_{DEM} is the time step in DEM, πR_{min} is the minimum particle size, and E and ν are the Young's modulus and Poisson's ratio of the particles, respectively. In general, the critical time step in DEM is much smaller than that in CFD. Therefore, the total stability condition is dominated by the DEM simulation. In the proposed model, Δt_{CFD} is set as 100 times that of Δt_{DEM} and the exchange of information between the DEM and CFD is performed at each step of CFD calculation.

Figure 1 shows the coupling procedures adopted in the CFD-DEM simulations. The detailed procedure during the

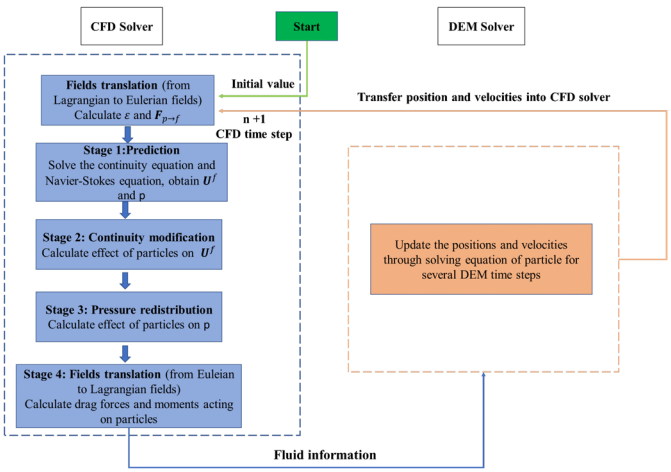

Fig. 1 (Color online) Scheme diagram of CFD-DEM coupling procedures

calculation was as follows: First, DEM data, including positions and velocities, were transferred into the CFD solver; then, a translation from the Lagrangian field to the Euler field was performed by the CFD solver, and the porosity ε and the interphase force between the fluid and particle $F_{p\to f}$ were updated according to the exchanged DEM data. Second, the velocity of the fluid U_f and pressure p were calculated using the continuity and Navier–Stokes equations. Third, U_f was modified by considering the influence of particles on the fluid, and the modified U_f was used to calculate the redistributed pressure. Finally, the drag force applied to the particle body was calculated using all updated parameters, and the CFD working step was temporarily paused, waiting for the DEM calculation step and data exchange. The drag force obtained in CFD was transferred to the DEM, and the resultant force of the particle was updated and used to calculate the new position and velocity of the particle. The coupling of CFD with the DEM was achieved using the commercial software Fluent for CFD and EDEM for the DEM [43].

2.2 Simulation study setup

The type and size of tritium breeders significantly affect the performance (e.g., porosity) of the solid blankets in fusion reactors. In most solid blanket designs, 1-mm-diameter Li_4SiO_4 particles are used as tritium breeders. A numerical sample of the Li_4SiO_4 pebble bed was prepared using the DEM code. Table 1 lists the physical properties of the Li_4SiO_4 particles and the key simulation parameters [44]. The boundary conditions [45] and the powder numbers are listed in Table 2.

Following material parameter determination, pebble-bed particles were generated using EDEM software. Slight compaction by the plate ensured close interactions between the breeding particles. As shown in Fig. 2, the CFD-DEM model

Table 1 Numerical parameters used in the simulation

Parameters	Value
DEM particle phase	
Particle diameter, d (mm)	1.0
Particle number	2454
Density (kg/m^3)	2323
Young's modulus (Gpa)	90
Poisson's ratio	0.24
Coefficient of friction	0.2
Coefficient of restitution	0.3
Domain size (mm^3)	12×12×15
CFD fluid phase	
Fluid density (kg/m^3)	0.1625
Fluid viscosity (Pa·s)	1.99×10^{-5}

Table 2 Boundary conditions

Boundary conditions	Value
Purge velocity (m/s)	0.1, 0.2, 0.3
Outlet pressure (kPa)	101
Powder number	500

measured 12 mm in length, 12 mm in width, and 15 mm in height. The velocity inlet was set as 5 mm above the pebble-bed surface to simulate the purge gas. A particle factory or a broken particle source was incorporated within an area measuring 8 mm × 8 mm × 1 mm at the top of the pebble beds. In the CFD-DEM model, the powders attempt to percolate through a fixed, nondeformable pebble bed under the influence of the purge gas.

The sizes of the powders produced by crushing Li_4SiO_4 pebbles cannot be uniformly distributed, and the powder flowability may change with the particle size (d_p) distribution. Table 3 lists the powder gradations and properties obtained from previous experimental and numerical studies [46]. In this study, three types of powder distributions were identified: fine, coarse, and well-graded particles. The powder grading table shows the mass percentages of various powder sizes. All powders were spherical, and the simulation settings and boundary conditions were consistent with those used for breeding particles. In EDEM software, each particle size gradation is depicted in four colors representing

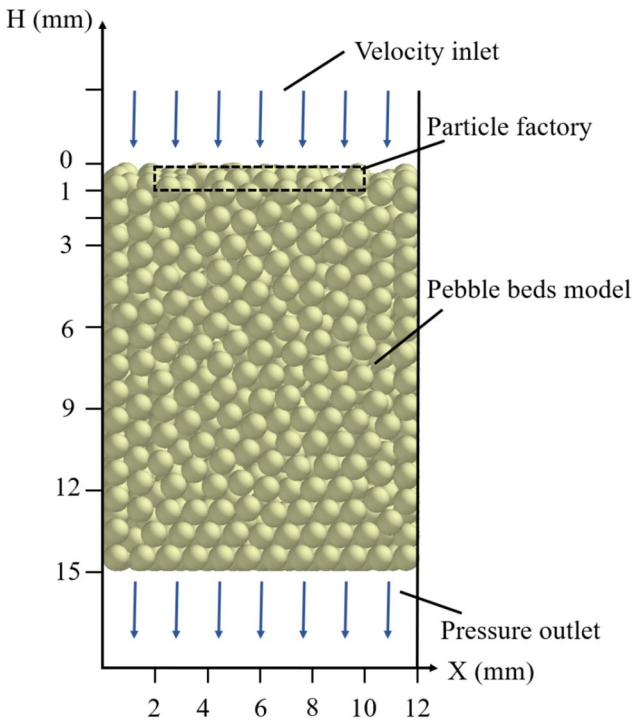

Fig. 2 (Color online) CFD-DEM model

Table 3 Particle size grading of powders

Powder size (mm)	Fine (%)	Coarse (%)	Well-graded (%)
0.08–0.12	55.46	0	29.47
0.12–0.16	44.54	0	25.74
0.16–0.20	0	51.92	23.29
0.20–0.24	0	48.08	21.50

Table 4 Cases of powder migration and clogging in pebble beds

Case	Purge velocity	Friction coefficient	Size distribution	Breeder orientation
1	0.1	0.1	Fine	χ
2	0.2	0.1	Fine	χ
3	0.3	0.1	Fine	χ
4	0.1	0.1	Well-graded	χ
5	0.1	0.1	Coarse	χ
6	0.3	0.1	Coarse	χ
7	0.1	0.2	Fine	χ
8	0.1	0.3	Fine	χ
9	0.1	0.1	Fine	ζ

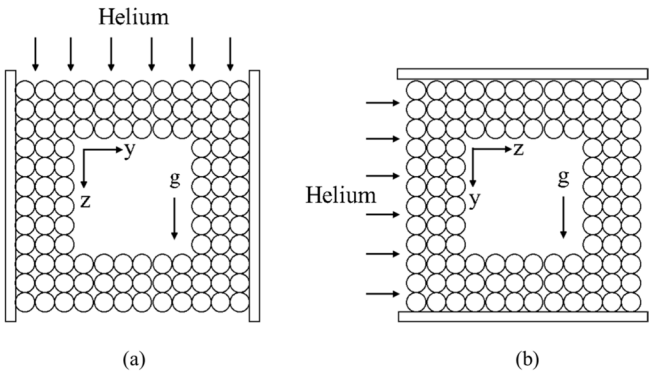

Fig. 3 Sketches of the two breeder orientations: **a** χ-configuration, **b** ζ-configuration

different sizes. For example, fine-powder sizes ranging from 0.08 mm to 0.16 mm are color-coded as green, yellow, pink, or red in the software. Powders smaller than 0.08 mm were excluded from the simulation owing to their small size and the extensive time required for generation.

Table 4 outlines the various cases and parameters: Cases 1–3 and 6 examined the purge velocity; Cases 1, 4, and 5 focused on the powder size distribution; Cases 1, 7, and 8 investigated the coefficient of friction; and Cases 1 and 9 compared the two breeder orientations. In this study, two ITER-relevant volumes were considered, as shown in Fig. 3. These volumes differed in their configurations according to the direction of gravity. Because of their similarity, we employed generic coordinate systems (χ, ζ). The ζconfiguration represents the TBM orientation of the EU [47], whereas the χ configuration aligns with several current TBM designs at ITER [48, 49].

2.3 Validation

2.3.1 Verification of the pebble-bed model

The specificity of a pebble bed mainly depends on the influence of the wall effect [30]. The classic mode of Klerk [50] was adopted to verify the validity of the porosity distribution along the x-axis for the pebble beds in this study. Local porosity is expressed as:

$$\varepsilon_r = \begin{cases} 2.14R^2 - 2.53R + 1 & R \leqslant 0.637 \\ \varepsilon_b + 0.29e^{-0.6R}\cos(2.3\pi(R-0.16)) + 0.15e^{-0.9R} & R > 0.637 \end{cases} \quad (11)$$

$$R = \frac{L}{d} \quad (12)$$

where R represents the dimensionless wall distance, d is the particle diameter, L is the box length, and ε_b is the porosity at the center of the pebble beds. Figure 4 shows the porosity along the x-axis direction of the DEM static pebble beds, calculated and compared using Eq. (11). The

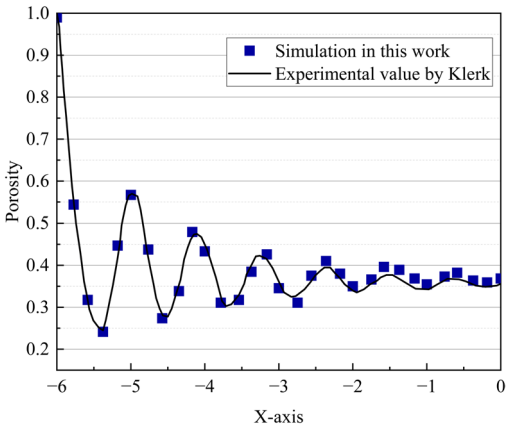

Fig. 4 (Color online) Porosity distribution of particles along the x-axis

results demonstrate the distinct oscillation characteristics of porosity within the pebble beds near the wall. The oscillation amplitude decreased along the radial direction and agreed closely with the experimental results. Therefore, the pebble-bed model obtained using DEM was considered valid for this study.

2.3.2 Verification of the CFD-DEM model

The Ergun equation [51] has been extensively employed to predict the pressure drops within pebble beds. This equation describes the relationship between the pressure drop and average velocity for the flow in the pebble beds:

$$\frac{|\Delta p|}{\Delta L} = 150\frac{(1-\varepsilon)^2}{\varepsilon^3}\frac{\mu}{d_c^2}V_{in} + 1.75\frac{1-\varepsilon}{\varepsilon^3}\frac{\rho}{d_c}V_{in}^2, \tag{13}$$

where $|\Delta p|$ is the pressure drop from inlet to outlet, ΔL is the height of the pebble bed, and V_{in} is the inlet gas velocity. To verify the constructed CFD-DEM model, the calculated results were compared with those of the Ergun equation. The comparison is shown in Fig. 5. A close agreement was observed, indicating that the proposed CFD-DEM model can accurately capture the behavior of particles and fluid flow.

3 Results and discussion

3.1 Law of powder transport and clogging in pebble beds

Figure 6 illustrates the migration and clogging processes of the powders with varying particle size distributions within the pebble beds. As shown in Fig. 6a, for Case 1, the surface-accumulated powders moved downward, driven by the purging gas, and their number gradually decreased. A large number

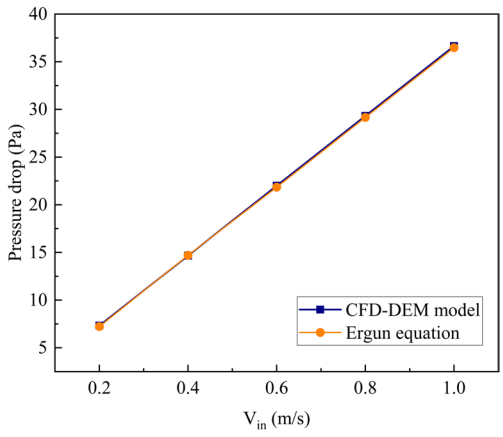

Fig. 5 (Color online) Comparison of the results of pressure drop in pebble beds

of particles accumulated in the upper pore structure of the pebble beds after running for 2 s. However, the distribution of powder in the pore structure decreased rapidly as the height of the pebble beds decreased. The distribution range of powder in the pebble beds was wide. Figure 6b shows that in Case 4, the smaller-sized surface-accumulated particles gradually migrated inward, driven by the purge gas. However, their migration distance was significantly shorter than that in Case 1, with most powder deposited at the upper part of the pebble beds and a smaller spread range. Figure 6c indicates that in Case 5, there was negligible vertical migration of surface-accumulated particles due to the purge gas, leading to significant accumulation at the upper part of the pore structure of the pebble beds.

Gerber et al. [52] observed that a decrease in the particle size ratio (d_p/d) resulted in clogging of the particles closer to the filler surface. A smaller ratio accelerated surface deposition and increased accumulation. With a smaller particle size ratio, the particles encounter similar-sized pores more frequently during transport, leading to earlier deposition and shallower clog depths. Continuous particle accumulation at these sites leads to clogging at shallower depths. The small particle size ratio caused the fine particles to clog only a thin layer of gravel pores near the surface of the pebble beds, hindering further permeation. The pebble-bed model features pores composed of larger pore bodies and smaller pore throats. Powders are captured in pores larger than or equal to their volume, irrespective of the particle size. Clogging can be distinguished by the presence of larger powder particles, which divide the clogged areas into zones A and B, as shown in Fig. 6a. Zone A contains large powder particles, whereas Zone B does not. The clogging mechanism of Zone A was: Red or pink particles initially settled within the pebble bed, predominantly in a shallow 5 mm layer. After forming a pore skeleton in the shallow pores of the pebble beds, the particles could not easily migrate again. This narrowing of the channels in the shallow layer facilitated the rapid accumulation of smaller-sized deposits. The clogging mechanism of Zone B was: Smaller powder particles, such as green particles, migrated and permeated inward through voids under the sweeping gas and gravity, eventually forming local deposits alongside larger particles.

Based on the two-dimensional images, Fig. 7 presents an analysis of the powder retention rate within the pebble beds. Considering the pebble-bed surface as the zero horizontal plane ($H = 0$), the distribution of the accumulated powder retention rate above depth H is defined as R_H

$$R_H = \frac{C_H}{C_t}, \tag{14}$$

where C_H is the powder content (g) in the part above depth H, and C_t is the initial total powder mass (g). Figure 7a shows the distribution of the accumulated retention rates

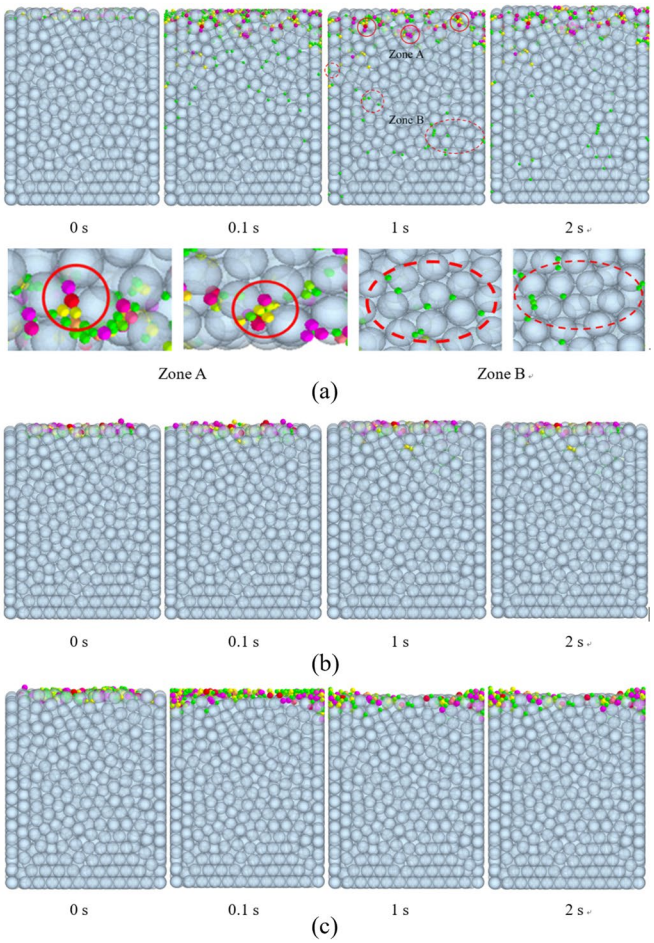

Fig. 6 (Color online) Migration and clogging process of powders of different grades in pebble beds. **a** Case 1, **b** Case 4, **c** Case 5

of the powders for different running times. Within 1 s, the vertical accumulation retention rate of the powder in the surface layer (1–5 mm) of the ball bed decreased, signifying gradual powder migration into the porous medium owing to purging. Beyond 1 s, the retention rate of the powder at the surface layer remained constant, indicating the stabilization of powder deposition in this area. From 1–2 s, a noticeable difference in the retention rate occurred in the middle layer (6–12 mm) of the pebble beds, but beyond 2 s, only minor changes were observed in the lower layer (12–15 mm), with the retention rate largely unchanged elsewhere. This result indicates that the powder deposition stabilized within the pebble beds, with clogging development progressing from top to bottom. Initially, the powder stabilized at the top of the pebble beds, followed by stable deposition in the middle and bottom regions.

Figure 7b shows the size grades. The disparity between well-graded and coarse powders was minimal. Both exhibited substantial deposition in the surface layer, with retention rates rapidly reaching 100%. In contrast, the fine powders demonstrated notable differences, characterized by deeper penetration. This minimal difference occurred because both well-graded and coarse powders contain particles larger than 0.16 mm. At equilibrium, these large particles clogged the surface pores of the pebble beds, hindering smaller particles in the well-graded powders from penetrating the surface, thus limiting any further increase in the retention rate. This result further confirms the two different clogging mechanisms mentioned in the analysis: One involves a powder with a large particle size and the other does not.

3.2 Effect of factors on powder migration development

3.2.1 Influence of powder size grading

Figure 8 illustrates the variation in the powder transport speed with size grading, representing the average speed of all powders. This result indicates a gradual decrease in powder transport speed over time. Ultimately, the powders became static in the pebble beds, with fine powders taking longer to settle than the well-graded and coarse powders. Furthermore, the powder transport speed increased with decreasing particle size, because smaller powders are more easily mobilized by fluid forces. The average speed of fine powders was 80% higher than that of well-graded and coarse

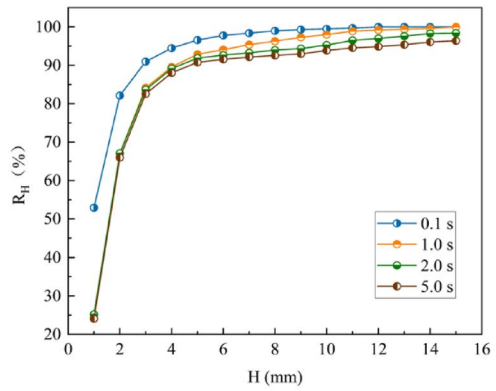

(a)

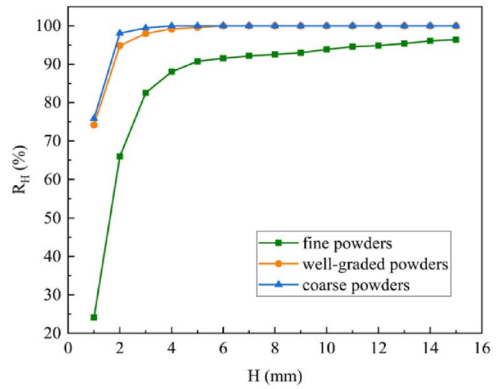

(b)

Fig. 7 (Color online) Distribution of accumulated retention rate of powders. **a** Different time points; **b** different size gradations

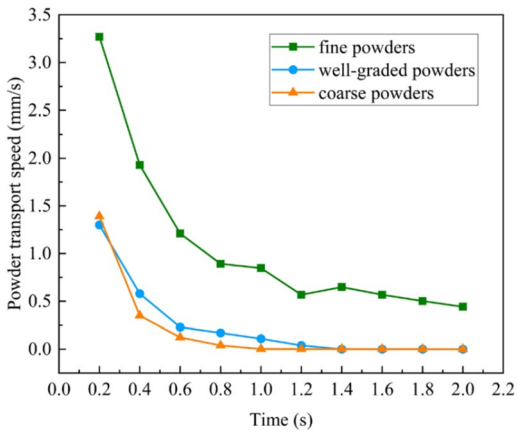

Fig. 8 (Color online) Transport speed of powders in different size grading

powders, highlighting the significant impact of large powders on the powder flow velocity in pebble beds. The results of dynamic migration and static clogging of the powder were similar; that is, the presence or absence of a large particle size had a significant influence on the dynamic migration process.

3.2.2 Influence of powder friction coefficient

Figure 9 shows the relationship between the average vertical velocity of the fine powders and changes in the friction coefficient. The changes in the average vertical velocity and transport speed were similar. As the friction coefficient increased, the average vertical velocity of the fine powder decreased significantly. According to the friction coefficient, ranging from low to high, the average vertical speeds were 1.09 mm/s, 0.43 mm/s, and 0.32 mm/s for the three cases. For powders with varying friction coefficients, the migration velocity followed a consistent pattern over time; it first decreased rapidly and then gradually approached a static state.

3.2.3 Influence of purge velocity

Figure 10 illustrates how the vertical velocity of the powders changed with the purge velocity, which was adjusted by controlling the outlet velocity. Figure 10a shows that the average vertical migration velocity of the powders tended to increase with increasing purge velocity. This effect is less pronounced than that of the size grading or friction coefficient because the purge velocity has a limited impact range of 0.07–0.2 mm/s, which is a factor of 4 smaller in magnitude. Furthermore, Fig. 10b demonstrates that the migration of the coarse powder was less affected by the purge velocity than that of the fine powder. Despite higher purge velocities,

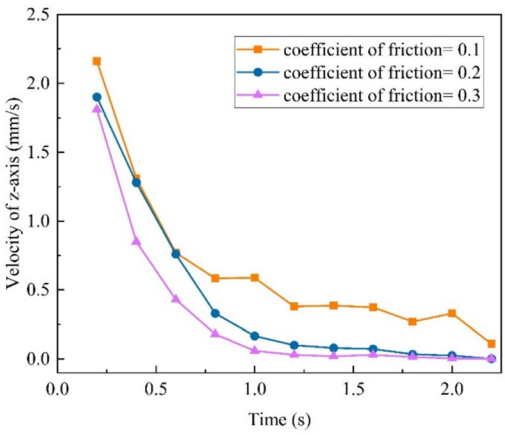

Fig. 9 (Color online) Vertical velocity of powders for different friction coefficients

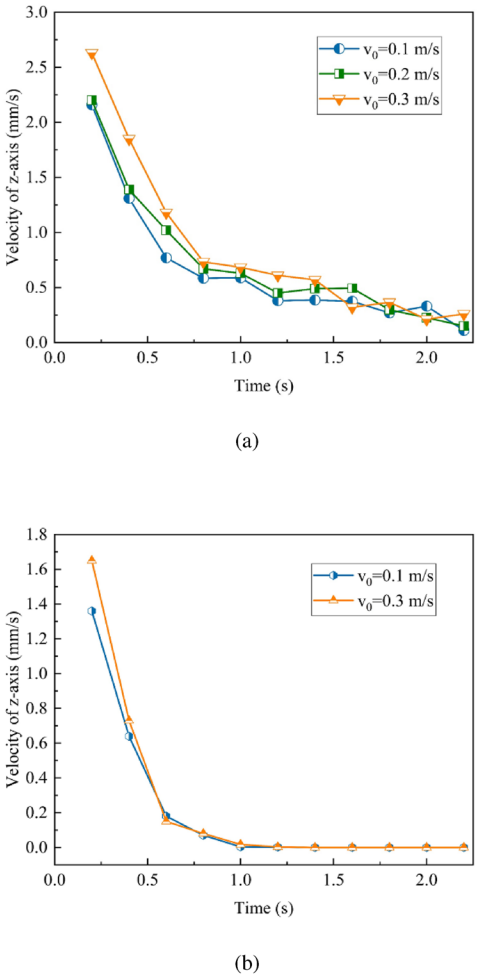

Fig. 10 (Color online) Vertical velocity of powders for different purge velocities: **a** fine powders and **b** coarse powders

it is challenging to mobilize large particles that cause clogging, indicating clogging stability. In summary, the impact of the purge velocity on powder migration in pebble beds was limited, and this effect varied significantly with different particle size ratios.

3.3 Study on stabilized powder distribution in clogged pebble beds

3.3.1 Distribution frequency of clogging powders in pebble beds

The powder clogging data from the final stability state were selected for analysis. Different colors, each corresponding to a unique powder size distribution, were extracted. The depth was segmented into 1 mm layers for statistical analysis. The ratio of the clogging powder in each layer to the total clogging powder was calculated. Figure 11 shows the dimensionless ratio N/N_0 normalized by N_0. This result illustrates the distribution of powders with a specific size grading, where N_0 is the total number of clogging powders and N represents the number of clogging particles in each layer. Powders of different sizes within the same layer were stacked. Figure 11a illustrates how the distribution frequency of fine powder changed across different layers during clogging. The red powder with d_p = 0.14–0.16 mm was distributed within the 0–4 mm range of the pebble beds. Pink powder, d_p = 0.12–0.14 mm, exhibited peak frequencies in the 0–3 mm range in the pebble beds, with most powders concentrated within 5 mm. The void structure of the surface layer of the spherical bed was blocked by large particles, and green and yellow powders (d_p = 0.08–0.12 mm) were primarily distributed in the 0–5 mm range of the pebble beds. However, the green and yellow powders still penetrated the interior and even the bottom of the pebble beds. Powder with a small particle size was more widely distributed in the pebble beds.

As shown in Fig. 11a–c, the coarse powder seldom invaded the middle part of the pebble-bed layers, whereas the fine powder penetrated the bottom. The fine powder was distributed more evenly at depth because the coarse powder prevents downward clogging. However, a comparison of well-graded and coarse powders revealed no significant differences in the concentration or invasion depth. A comparison between Fig. 11a, d shows that under varying purge velocities, larger powder particles (> 0.14 mm) primarily settled in the surface layer of the pebble beds, whereas smaller particles (< 0.12 mm) were distributed more evenly throughout the middle and lower sections. From the superposition of the frequency distribution, with a purge velocity of 0.1 m/s, the clogging powder in the 0–3 mm region of the pebble beds constituted 76% of the total powder. At a purge velocity of 0.2 m/s, the clogging powder in the 0–3 mm area represented 81% of the total powder, with pink powder (d_p = 0.12–0.14 mm) present in the middle part of the pebble beds. The results indicate that the powder penetration depth and quantity into the pores increased with increasing purge velocity. Comparing Fig. 11a, e shows that as with increasing friction coefficient, the peak distribution frequency of the clogging powder also increased. In Case 1, 63% of the powder was clogged in the surface layer of the pebble beds (0–2 mm), and in Case 7, this value increased to 69%. Powder with larger particles predominantly clogged the surface layer, whereas smaller particles penetrated the bottom layer. This result demonstrates that the friction coefficient significantly affects powders with larger surface areas, with a minimal effect on smaller powders.

3.3.2 Effect of breeder orientation on powder migration and clogging

Figure 12 illustrates the impact of various proliferation orientations on powder migration and clogging. Figure 12b

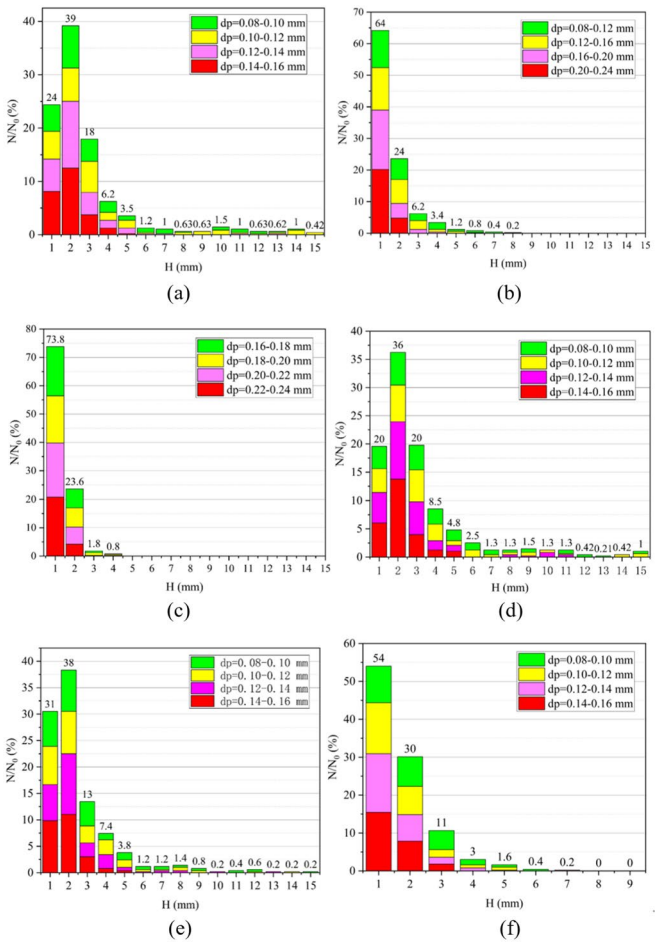

Fig. 11 (Color online) The distribution frequency of clogging powders in pebble beds. **a** Case 1, **b** Case 4, **c** Case 5, **d** Case 2, **e** Case 7, **f** Case 9

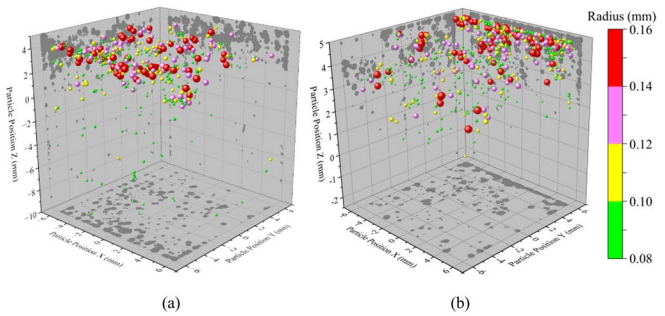

Fig. 12 (Color online) Three-dimensional distribution of clogging powders with different breeder orientations. **a** Case 1, **b** Case 9

reveals that in the ζ configuration, the powder near the upper wall (Y= −6 mm) moved downward away from the top wall, with significant deposits forming as powders from the middle rolled down to the lower wall area ($Y = 6$ mm). In contrast, the pebble beds in the χ configuration exhibited distinct powder migration and sedimentation patterns. Figure 12a shows that the powder near the wall settled in the same post-migration area, which is a trend observed in other areas of the pebble beds. When the breeder particles in the pebble beds are crushed, they fall owing to gravity and fluid force, yet maintain their general direction. Comparing Fig. 11f and (a) shows that the powder in the ζ configuration predominantly settled in the 0–5 mm region in the upper part of the pebble beds, and the quantity of deposited powder sharply decreased with decreasing height.

3.4 Characterization and developmental stages of migration and clogging

The migration and clogging of powder in pebble beds significantly impact the system and are influenced by various factors. Complex dynamics of the powder behavior in

the pebble beds were observed. The influence of different parameters on the dynamic behavior of the powder varied. To characterize the powder behavior, including the migration distance and velocity, we defined the migration efficiency $v^*(l,v)$. From prior analysis and with the purging gas parameters in the fixed ball bed established, the factors affecting $v^*(l,v)$, in descending order of significance, were the powder size distribution S, breeder orientation of the pebble beds g, friction coefficient f, and average purge velocity V. Furthermore, parameters not investigated in this study, such as the particle size and temperature, may also affect powder migration. These effects were uniformly classified as other factors (oth). Thus, the migration efficiency $v^*(l,v)$ is characterized as:

$$v^*(l,v) = f(S,g,f,V,oth). \tag{15}$$

By analyzing the average transport velocity at various times, we observed the behavior of powder migration within the 0.2–5.0 s range. Powder migration velocity in the pebble beds between 0.2 and 5.0 s was normalized. Figure 13a illustrates that the powder migration velocity can be categorized into three phases: rapid decay, linear decay, and stability. During the 0.2–5.0 s period, the average velocity of powder decreased rapidly (rapid decay stage) first, followed by a linear decrease in the rate of change (linear decay stage), culminating in stabilization. Stages 1, 2, and 3 were modeled using polynomial and linear analyses:

Stage 1:

$$v_{n1} = a_1x^2 + b_1x + c_1, \tag{16}$$

Stage 2:

$$v_{n2} = d_1x + e_1, \tag{17}$$

Stage 3:

$$v_{n3} \to 0^+. \tag{18}$$

In this paper, v_{n1} represents the normalized migration velocity during Phase 1, v_{n2} during Phase 2, and v_{n3} during Phase 3. The parameters in Eqs. (16) and (17) vary according to their boundary conditions. Taking Case 1 as an example, under conditions such as a purge velocity of 0.1 m/s, a friction coefficient of 0.1, and the fine-powder size distribution, the values of a_1, b_1, c_1, d_1, and e_1 were, respectively, 1.1024, −2.2963, 1.3778, −0.0786, and 0.2935.

Following powder stabilization ($v \to 0^+$), we analyzed the powder clogging trends at different locations within the pebble beds. Figure 13b shows that the 0–4 mm depth was the predominant area for powder retention. Clogging can be classified into two categories: extensive superficial and uniform internal. Initially, the retention rate in the 0–4 mm range increased quickly, indicating extensive surface

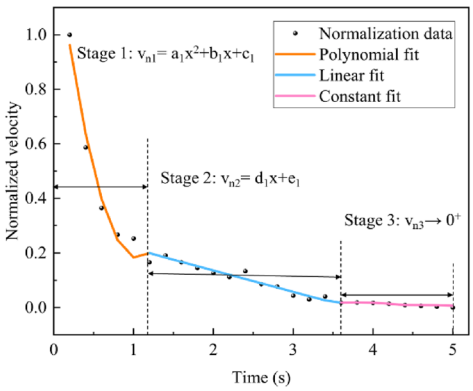

(a)

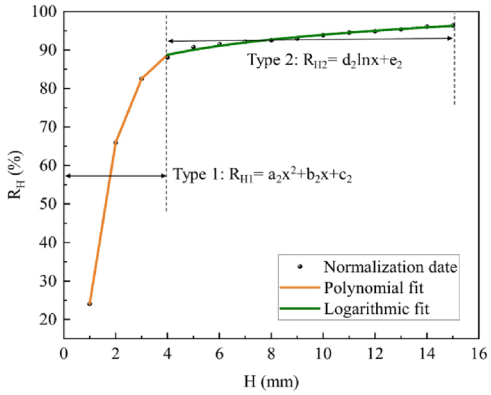

(b)

Fig. 13 (Color online) Normalized analysis of migration and clogging development

deposition blockage. This stage was followed by a gradual and consistent change in the retention rate, suggesting uniform internal deposition of fine-grained powder. Types 1 and 2 were fitted with polynomial and logarithmic analyses, respectively:

Type 1:

$$R_{H1} = a_2x^2 + b_2x + c_2, \tag{19}$$

Type 2:

$$R_{H2} = d_2\ln x + e_2. \tag{20}$$

The parameters in Eqs. (19) and (20) changed according to the boundary conditions. For Case 1, with a purge velocity of 0.1 m/s, friction coefficient of 0.1, and fine-powder size distribution, the values of a_2, b_2, c_2, d_2, and e_2 were −9.085, 66.267, −32.37, 0.5646, and 88.098, respectively.

4 Conclusion

In this study, a two-way coupled CFD-DEM calculation was employed to analyze the powder migration and clogging mechanisms within pebble beds. The governing equations, establishment of the CFD-DEM model, validation, and coupling process are detailed in this paper. The effects of the breeder orientation, purge velocity, particle size grading, and friction coefficient on powder migration and clogging were assessed through numerical calculations. The powder migrated within the pebble beds owing to the fluid force. With increasing purge velocity, fine powder penetrated deeper into the pebble beds, in contrast to coarse powder, which showed less sensitivity to this effect. Increases in the friction coefficient and powder size distribution led to increased powder accumulation in the top layer of the pebble beds. The powder migration progressed from top to bottom, with the powder near the upper layer stabilizing first and then developing downward. Two migration and clogging mechanisms were identified: one involves powder with a large particle size, and the other does not. The first mechanism is more common and rapidly develops. The powder size distribution significantly influenced the migration depth; coarser layers tended to block the surface, whereas finer particles reached the lower parts of the pebble beds. The breeder orientation of pebble beds significantly impacted migration clogging: In the ζ configuration, the powder moved in the direction of gravity, away from the upper wall, forming extensive deposits on the lower wall. Various parameters influence powder migration and clogging behavior within pebble beds. Excluding time, the sensitivity ranks from highest to lowest are powder size distribution (S), breeder orientation of the pebble beds (g), friction coefficient (f), and average purge velocity (V).

From the analysis, a formula is proposed to characterize the behavior of the powder in the pebble beds: $v^*(l,v) = f(S,g,f,V,oth)$. Powder migration velocity development is categorized into three stages: rapid decay stage, linear decay stage, and stable, analyzed and fitted with normalization and formulas. The clogging in the pebble beds is categorized into two types depending on their distribution: extensive superficial clogging and uniform internal clogging, with the process modeled using formulas. The fitted curve was utilized to depict the tendency of migration and clogging, and numerical analyses culminated in the development of a model depicting powder migration and clogging behaviors.

For simplicity, all powders were modeled as spheres in this study, although real-world powder particles are irregularly shaped. Despite these simplifications, the findings of this study offer valuable general conclusions, particularly because the input parameters mirror those of actual pebble beds. Consequently, the results of this study can provide an effective reference for further research on powder dynamics and pebble bed properties in packed beds and provide ideas for the design of blankets for fusion reactors.

Author contributions All authors contributed to the study conception and design. Material preparation, data collection and analysis were performed by Xue-Tao Cui, Qi-Gang Wu and Jian Wang. The first draft of the manuscript was written by Xue-Tao Cui, and all authors commented on previous versions of the manuscript. All authors read and approved the final manuscript.

Data availability The data that support the findings of this study are openly available in Science Data Bank at https://cstr.cn/31253.11.sciencedb.28744 and https://www.doi.org/10.57760/sciencedb.28744

Declarations

Conflict of interest The authors declare that they have no Conflict of interest.

References

1. G. Federici, W. Gilbert, M.R. Gilbert et al., European DEMO design strategy and consequences for materials. Nucl. Fusion **57**, 092002 (2017). https://doi.org/10.1088/1741-4326/57/9/092002
2. S. Cui, D. Zhang, Q. Lian et al., Evaluation and optimization of tritium breeding, shielding and nuclear heating performances of the helium cooled solid breeder blanket for CFETR. Int. J. Hydrogen Energy **42**, 24263–24277 (2017). https://doi.org/10.1016/j.ijhydene.2017.07.215
3. B.P. Gong, Y. Feng, H. Liao et al., Discrete element modeling of pebble beds packing structures for HCCB TBM. Fusion Eng. Des. **121**, 256–264 (2017). https://doi.org/10.1016/j.fusengdes.2017.08.002
4. M. Holelzl, G.T.A. Huijsmans, S.J.P. Pamela et al., The JOREK non-linear extended MHD code and applications to large-scale instabilities and their control in magnetically confined fusion plasmas. Nucl. Fusion **61**, 065001 (2021). https://doi.org/10.1088/1741-4326/abf99f
5. T. Donné, Y. Liang, MHD control in burning plasmas. Nucl. Fusion **52**, 070201 (2012). https://doi.org/10.1088/0029-5515/52/7/070201
6. D. Liu, W.X. Tian, G.H. Su et al., Experimental study on helium pressure drop across randomly packed bed for fusion blanket. Fusion Eng. Des. **112**, 47–51 (2017). https://doi.org/10.1016/j.fusengdes.2017.09.009
7. D. Mandal, N. Kulkarni, S. Gosavi et al., Experimental investigation of effective thermal conductivity of packed lithium-titanate pebble bed with external heat source and flow of helium. Fusion Eng. Des. **115**, 56–66 (2017). https://doi.org/10.1016/j.fusengdes.2016.12.035
8. N. Nemati, P. Andersson, V. Stenberg et al., Experimental investigation of the effect of random packings on heat transfer and particle segregation in packed-fluidized bed. Ind. Eng. Chem. Res. **60**, 10365–10375 (2021). https://doi.org/10.1021/acs.iecr.1c01221
9. N. De, A. Singh, Numerical simulation of particle migration in suspension flow through heterogeneous porous media. Part. Sci. Technol. **39**, 19–31 (2021). https://doi.org/10.1080/02726351.2019.1651806

10. Q.H. Feng, L. Cha, C. Dai et al., Effect of particle size and concentration on the migration behavior in porous media by coupling computational fluid dynamics and discrete element method. Powder Technol. **360**, 704–714 (2020). https://doi.org/10.1016/j.powtec.2019.10.011
11. Y. Lee, D.K. Choi, S.P. Hwang et al., Numerical investigation of purge gas flow through binary-sized pebble beds using discrete element method and computational fluid dynamics. Fusion Eng. Des. **158**, 111704 (2020). https://doi.org/10.1016/j.fusengdes.2020.111704
12. Z.X. Wu, Y.W. Wu, C.L. Wang et al., Experimental and numerical study on helium flow characteristics in randomly packed pebble bed. Ann. Nucl. Energy **128**, 268–277 (2019). https://doi.org/10.1016/j.anucene.2019.01.016
13. Y.J. Li, T.H. Ye, P.H. Zhao et al., Study on the dynamic behavior of solid breeder materials and neutron multipliers under the perturbation of the magnetic field. Fusion Eng. Des. **160**, 111924 (2020). https://doi.org/10.1016/j.fusengdes.2020.111924
14. B. Ji, S. Gu, Q. Qi et al., Effect of γ ray irradiation on thermal conductivity of tritium breeding material Li_2TiO_3. Ceram. Int. **47**, 11481–11490 (2021). https://doi.org/10.1016/j.ceramint.2020.12.276
15. J.T.V. Lew, A. Ying, M. Abdou, Numerical study on influences of bed resettling, breeding zone orientation, and purge gas on temperatures in solid breeders. Fusion Eng. Des. **109**, 539–544 (2016). https://doi.org/10.1016/j.fusengdes.2016.02.059
16. Q. Liu, B. Zhao, J.C. Santamarina, Particle migration and clogging in porous media: a convergent flow microfluidics study. J. Geophys. Res. **124**, 9495–9504 (2019). https://doi.org/10.1029/2019JB017813
17. X. Ye, R. Cui, X. Du et al., Mechanism of suspended kaolinite particle clogging in porous media during managed aquifer recharge. Groundwater **57**, 764–771 (2019). https://doi.org/10.1111/gwat.12872
18. G.F. Hua, W. Zhu, L.F. Zhao et al., Clogging pattern in vertical-flow constructed wetlands: Insight from a laboratory study. J. Hazard. Mater. **180**, 668–874 (2010). https://doi.org/10.1016/j.jhazmat.2010.04.088
19. J. Zhang, G. Ma, Z. Dai et al., Numerical study on pore clogging mechanism in pervious pavements. J. Hydrol. **565**, 589–598 (2018). https://doi.org/10.1016/j.jhydrol.2019.124049
20. C.F. Yong, D.T. McCarthy, A. Deletic, Predicting physical clogging of porous and permeable pavements. J. Hydrol. **481**, 48–55 (2013). https://doi.org/10.1016/j.jhydrol.2012.12.009
21. S.A. Tan, T.F. Fwa, C.T. Han, Clogging evaluation of permeable bases. J. Transp. Eng. **129**, 309–315 (2003). https://doi.org/10.1061/(asce)0733-947x(2003)129:3(309)
22. Q. Sun, W. Peng, S. Yu et al., A review of HTGR graphite dust transport research. Nucl. Eng. Des. **360**, 110477 (2020). https://doi.org/10.1016/j.nucengdes.2019.110477
23. J. Moghadasi, H. Müller-Steinhagen, M. Jamialahmadi et al., Theoretical and experimental study of particle movement and deposition in porous media during water injection. J. Petrol. Sci. Eng. **43**, 163–181 (2004). https://doi.org/10.1016/j.petrol.2004.01.005
24. M. Turco, R. Kodešová, G. Brunetti et al., Unsaturated hydraulic behaviour of a permeable pavement: Laboratory investigation and numerical analysis by using the HYDRUS-2D model. J. Hydrol. **554**, 780–791 (2017). https://doi.org/10.1016/j.jhydrol.2017.10.00
25. J. Huang, J. He, C. Valeo et al., Temporal evolution modeling of hydraulic and water quality performance of permeable pavements. J. Hydrol. **533**, 15–27 (2016). https://doi.org/10.1016/j.jhydrol.2015.11.042
26. R. Pieralisi, S.H.P. Cavalaro, A. Aguado, Advanced numerical assessment of the permeability of pervious concrete. Cem. Concr. Res. **102**, 149–160 (2017). https://doi.org/10.1016/j.cemconres.2017.09.009
27. Y. Tsuji, T. Kawaguchi, T. Tanaka, Discrete particle simulation of two-dimensional fluidized bed. Powder Technol. **77**, 79–87 (1993). https://doi.org/10.1016/0032-5910(93)85010-7
28. Y. Hou, W. Sun, P. Das et al., Coupled Navier-Stokes phase-field model to evaluate the microscopic phase separation in asphalt binder under thermal loading. J. Mater. **28**, 2364–2369 (2016). https://doi.org/10.1061/(asce)mt.1943-5533.0001581
29. J.D. Zhao, T. Shan et al., Coupled CFD-DEM simulation of fluid-particle interaction in geomechanics. Powder Technol. **239**, 248–258 (2013). https://doi.org/10.1016/j.powtec.2013.02.003
30. B.R. Zhang, Z.Y. Xia, Z.W. Zhou et al., DEM-CFD coupled simulation for determination of character of heat and mass transfer and purge gas flow in Li_4SiO_4 Pebble Bed. Atom. Energy Sci. Technol. **55**, 1367–1375 (2021). https://doi.org/10.7538/yzk.2020.youxian.0924
31. T. Eppinge, K. Seidler, M. Kraume, DEM-CFD simulations of fixed bed reactors with small tube to particle diameter ratios. Powder Technol. **166**, 324–331 (2013). https://doi.org/10.1016/j.cej.2010.10.053
32. L. Chen, Y.H. Chen, K. Huang et al., Investigation of effective thermal conductivity for pebble beds by one-way coupled CFD-DEM method for CFETR WCCB. Fusion Eng. Des. **106**, 1–8 (2016). https://doi.org/10.1016/j.fusengdes.2016.03.001
33. H. Wu, N. Gui, X.T. Yang et al., A smoothed void fraction method for CFD-DEM simulation of packed pebble beds with particle thermal radiation. Int. J. Heat. Mass. Tran. **118**, 275–288 (2018). https://doi.org/10.1016/j.ijheatmasstransfer.2017.10.123
34. Z.Y. Zhou, S.B. Kuang, K.W. Chu et al., Discrete particle simulation of particle-fluid flow: Model formulations and their applicability. J. Fluid Mech. **661**, 482 (2010). https://doi.org/10.1017/S002211201000306X
35. C.T. Crowe, J.D. Schwarzkopf, M. Sommerfeld et al., *Multiphase Flows with Droplets and Particles*, 2nd edn. (CRC Press, Boca Raton, FL, 2011)
36. M.W. Schmeeckle, Numerical simulation of turbulence and sediment transport of medium sand. J. Geophys. Res. Earth Surf. **119**, 1240 (2014). https://doi.org/10.1002/2013JF002911
37. R. Sun, H. Xiao, SediFoam: A general-purpose, open-source CFD-DEM solver for particle-laden flow with emphasis on sediment transport. Comput. Geosci. **89**, 207 (2016). https://doi.org/10.1016/j.cageo.2016.01.011
38. K. Luo, F. Wu, S. Yang, CFD–DEM study of mxing and dispersion behaviors of solid phase in a bubbling fluidized bed. Powder Technol. **274**, 482–493 (2015). https://doi.org/10.1016/j.powtec.2015.01.046
39. D. Gidaspow, *Multiphase Flow and Fluidization: Continuum and Kinetic Theory Descriptions* (Springer, New York, 1994), p.467
40. C.Y. Wen, Y.H. Yu, A generalized method for predicting the minimum fluidization velocity. AIChE J. **12**, 610–612 (1966). https://doi.org/10.1002/aic.690120343
41. S. Ergun, A.A. Orning, Fluid flow through randomly packed columns and fluidized beds. Ind. Eng. Chem. **41**, 1179–1184 (1949). https://doi.org/10.1021/ie50474a011
42. T. Li, Y. Xu, C. Thornton, A comparison of discrete element simulations and experiments for 'sandpiles' composed of spherical particles. Powder Technol. **160**, 219–228 (2005). https://doi.org/10.1016/j.powtec.2005.09.002
43. L. Li, B. Li, Implementation and validation of a volume-of-fluid and discrete-element-method combined solver in OpenFOAM. Particuology. **39**, 109–115 (2018). https://doi.org/10.1016/j.partic.2017.09.007
44. J. Wang, M.Z. Lei, H. Yang et al., Study on the packing characteristics of a special "J'' shape ceramic packed pebble bed based

on discrete element modeling. Powder Technol. **379**, 362–372 (2021). https://doi.org/10.1016/j.powtec.2020.10.076
45. J. Wang, M. Liu, M. Lei et al., Gas and powder flow characteristics of packed bed: a two-way coupled CFD-DEM study. Int. J. Multiphase. Flow. **178**, 104904 (2024). https://doi.org/10.1016/j.ijmultiphaseflow.2024.104904
46. M. Lei, Q. Wu, S. Xu et al., Crushing behaviour of Li_4SiO_4 and Li_2TiO_3 ceramic particles. Nucl. Mater. Energy. **31**, 101188 (2022). https://doi.org/10.1016/j.nme.2022.101188
47. F. Hernández, M. Kolb, M. Ilić et al., Set-up of a pre-test mock-up experiment in preparation for the HCPB Breeder Unit mock-up experimental campaign. Fusion Eng. Des. **88**, 2378–2383 (2013). https://doi.org/10.1016/j.fusengdes.2013.02.107
48. S. Cho, M.Y. Ahn, D.H. Kim et al., Current status of design and analysis of Korean helium-cooled solid breeder test blanket module. Fusion Eng. Des. **83**, 1163–1168 (2008). https://doi.org/10.1016/j.fusengdes.2008.05.037
49. K.M. Feng, C.H. Pan, G.S. Zhang et al., Progress on design and R&D for helium-cooled ceramic breeder TBM in China. Fusion Eng. Des. **87**, 1138–1145 (2012). https://doi.org/10.1016/j.fusengdes.2012.02.098
50. A.D. Klerk, Voidage variation in packed beds at small column to particle diameter ratio. AIChE J. **49**, 2022–2029 (2003). https://doi.org/10.1002/aic.690490812
51. S. Ergun, Fluid flow through packed columns. Chem. Eng. Prog. **48**, 89–94 (1952)
52. G. Gerber, S. Rodts, P. Aimedieu et al., Particle-size-exclusion clogging regimes in porous media. Phys. Rev. Lett. **120**, 1179–1184 (2018). https://doi.org/10.1103/physrevlett.120.148001